# Direct numerical simulation of gas-liquid mass transfer around a spherical contaminated bubble in the stagnant-cap regime

Kalyani Kentheswaran, Nicolas Dietrich, Sébastien Tanguy, Benjamin Lalanne

# Direct numerical simulation of gas-liquid mass transfer around a spherical contaminated bubble in the stagnant-cap regime

Kalyani Kentheswaran[a,b,d,*], Nicolas Dietrich[a,d], Sébastien Tanguy[c,d] and Benjamin Lalanne[b,d,**]

[a]Toulouse Biotechnology Institute, Université de Toulouse, CNRS, INRAE, INSA, Toulouse, France
[b]Laboratoire de Génie Chimique, Université de Toulouse, CNRS, INP, UPS, Toulouse, France
[c]Institut de Mécanique des Fluides de Toulouse, Université de Toulouse, CNRS, INP, UPS, Toulouse, France
[d]Fédération de recherche FERMaT, CNRS, Toulouse, France

ARTICLE INFO

*Keywords*:
Mass transfer
Direct numerical simulation
Rising bubbles
Surfactants
Stagnant-cap regime

ABSTRACT

Direct Numerical Simulations are performed to investigate the gas-liquid mass transfer around a rising spherical bubble contaminated by insoluble surfactants. The surfactant transport on the bubble surface and the Marangoni effect are taken into account when solving the hydrodynamics, resulting in the stagnant-cap condition. A parametric study is carried out to investigate the mass transfer by varying the Reynolds, Marangoni and Schmidt numbers. A thorough analysis of the impact of surfactants on the bubble hydrodynamics is presented through a correlation for the maximum velocity $u^*_{max}$ along the interface as a function of the contamination angle $\theta_{cap}$. These two parameters are then found to be crucial to quantify the rate of mass transfer around the interface. The latter is analyzed through the Sherwood number, which decreases when the interface is partially immobilized, between the value for a clean bubble and a solid sphere. A local analysis of the mass flux is carried out, which shows that the boundary layer thickens around the immobilized zone of the interface, and that the transfer rate in the mobile zone is also lower than for a clean bubble at same $Re$, both effects resulting in a decrease of the global $Sh$. The latter is in particular very sensitive to the local hydrodynamic condition in the front part of the interface, where the flux is locally higher and which can be characterized by the intensity of the maximum surface velocity. Finally, a correlation is proposed to predict the Sherwood number of a contaminated bubble depending on both global ($Re$, $Sc$) and local ($\theta_{cap}$, $u^*_{max}$) parameters, with a large range of validity ($1 \leq Re \leq 100$, $1 \leq Sc \leq 500$, $0 \leq \theta_{cap} \leq \pi$) based on a comparison with previous numerical studies.

## 1. Introduction

The performances and intensification of many industrial processes using bubble columns or chemical reactors are directly related to the phenomenon of gas-liquid mass transfer. Predicting the transfer rate between the two phases in such configurations rich of contaminants or surfactants is therefore of high interest, but complex. An inclusion passing through a medium with impurities becomes easily contaminated with a small amount of surfactants, which decrease its translation velocity to the one of a solid sphere of same size, as observed in various experimental and numerical studies [9, 3, 55, 42, 52] even when the surface tension is not significantly affected [27]. Frumkin and Levich [19, 33] identified the surface tension gradient resulting from the surfactants advection due to the bubble motion, to account for the velocity decrease. From this gradient appears an interfacial stress resisting to the bubble motion known as the Marangoni force, which tends to smooth this gradient as shown in figure 1. Advected surfactants at the bubble rear form a stagnant cap where the interface velocity is zero (zone of immobile interface), as Horton et al. [22] observed in their experimental results through the circulation motion inside drops in the presence of impurities; along this immobile zone, the surface tension is lowered. Reversely, the front part is free of surfactants, the flow satisfies a slip condition (zone of mobile interface) and the surface tension is locally higher. Pesci et al. [44] proposed a computational analysis of a rising bubble influenced by soluble surfactants and pointed out the significant impact of the surfactant concentration and the initial surface contamination on the terminal velocity and the bubble path. As mentioned by Palaparthi et al. [42], soluble surfactants adsorb from the liquid to the bubble surface, then are swept from the front to the trailing pole where the locally high concentration of surfactants leads to desorption. Therefore, a steady-state kinetics can be reached where the adsorption flux globally balances the desorption flux. When the rate of surface convection of surfactants is much higher than their rate of exchange with the bulk and that of surface diffusion, the stagnant-regime is obtained, characterized by a contamination angle $\theta_{cap}$. Such a stagnant-cap regime can also be obtained with a simulation which deals with insoluble surfactants, i.e. by neglecting any transfer of surfactant from or to the bulk (the total mass of adsorbed surfactants at the interface is thereby constant in the simulation), by considering their surface transport and the interfacial Marangoni force [33, 11]. The latter approach is used in this investigation.

In the creeping flow regime, Sadhal and Johnson [49] have quantified the rising velocity decrease and proposed an analytical relation between the contamination angle $\theta_{cap}$ and the reduced drag coefficient $C^*_D$ defined from the clean bub-

*Corresponding author
**Principal corresponding author
kalyani.kentheswaran@toulouse-inp.fr (K. Kentheswaran); benjamin.lalanne@ensiacet.fr (B. Lalanne)
ORCID(s):

## Nomenclature

| | |
|---|---|
| $\Delta_s$ | surface laplacian |
| $\nabla_s$ | surface gradient |
| **Subscripts** | |
| $gas$ | gas side properties or variables |
| $liq$ | liquid side properties or variables |
| $s$ | surface or tangential variables |
| **Constants** | |
| $\sigma_0$ | surface tension in a clean configuration ($N.m^{-1}$) |
| $\vec{g}$ | gravitational acceleration ($m.s^{-2}$) |
| $D_s$ | surfactant surface diffusion coefficient ($m^2.s^{-1}$) |
| $l_r$ | domain radial length (m) |
| $l_z$ | domain longitudinal length (m) |
| $R_g$ | gas constant ($J.mol^{-1}.K^{-1}$) |
| $T$ | temperature (K) |
| **Dimensionless numbers** | |
| $Ar$ | Archimedes number |
| $C_D$ | drag coefficient |
| $C_D^*$ | normalized drag coefficient |
| $Ma$ | Marangoni number |
| $Pe$ | Péclet number |
| $Pe_{max}$ | Péclet number based on the maximum interface velocity |
| $Re$ | Reynolds number |
| $Sc$ | Schmidt number |
| $Sh$ | Sherwood number |
| $Sh^*$ | normalized Sherwood number |
| $u_{max}^*$ | dimensionless maximum interface velocity |
| $We$ | Weber number |
| **Properties** | |
| $\bar{\sigma}$ | average surface tension ($N.m^{-1}$) |
| $\mu$ | dynamic viscosity (Pa.s) |
| $\rho$ | density ($kg.m^{-3}$) |
| $\sigma$ | surface tension ($N.m^{-1}$) |
| **Superscripts** | |
| $clean$ | case of a clean bubble |
| $solid$ | case of a solid sphere |
| **Variables** | |
| $\bar{\bar{D}}$ | deformation tensor |
| $\bar{\Gamma_0}$ | initial average surfactants concentration ($mol.m^{-2}$) |
| $\bar{\Gamma}$ | average surfactants concentration ($mol.m^{-2}$) |
| $\delta_h$ | thickness of the hydrodynamics boundary layer (m) |
| $\delta_m$ | thickness of the mass boundary layer (m) |
| $\Gamma$ | surfactants concentration field ($mol.m^{-2}$) |
| $\kappa$ | interface curvature |
| $\phi$ | level set function |
| $\theta_{cap}$ | angle of contamination (rad) |
| $\vec{n}$ | interface normal vector |
| $\vec{u}$ | velocity field ($m.s^{-1}$) |
| $\vec{u}_{int}$ | interface velocity ($m.s^{-1}$) |
| $\widetilde{\Gamma}$ | extrapolation field of the surfactants concentration ($mol.m^{-2}$) |
| $C$ | solute concentration field ($mol.m^{-3}$) |
| $D$ | diffusion coefficient ($m^2.s^{-1}$) |
| $d$ | bubble diameter (m) |
| $p$ | pressure field (Pa) |
| $R$ | bubble radius (m) |
| $U_\infty$ | terminal rising velocity ($m.s^{-1}$) |
| $U_c$ | characteristic convection velocity ($m.s^{-1}$) |
| $u_{max}$ | maximum interface velocity ($m.s^{-1}$) |
| $u_s$ | tangential velocity ($m.s^{-1}$) |

ble and the solid sphere coefficients, the latter corresponding to a bubble with a fully-immobile interface. Cuenot et al. [11] investigated on the transient evolution of a bubble contaminated by soluble surfactants at high Reynolds numbers and obtained a close behaviour of the reduced drag coefficient as [49] despite the different hydrodynamic conditions. The same results were observed in the numerical investigation of Piedfert et al. [45] for a droplet contaminated by insoluble surfactants and rising in another liquid, at high Reynolds number and low density and viscosity ratios.

Under clean conditions, correlations of the mass transfer around a rising bubble are given in various studies, such as Clift et al. [9] under creeping flow conditions, Lochiel and Calderbank [34] for spherical and spheroidal bubbles at high Schmidt and Péclet numbers, Takemura and Yabe [53] for high Reynolds and Péclet numbers. Based on previous numerical studies [13, 48, 17], Colombet et al. [10] proposed a more general correlation of the Sherwood number, valid for a wide range of Péclet and Reynolds numbers. This prediction is based on the maximum Péclet number calculated from the maximum interface velocity which characterizes the mass transfer rate around a clean and rising bubble in the most accurate way, according to the authors. The impact of surfactants is generally not considered in mass transfer models, whereas significant effects were observed in both experiments and numerical simulations. Indeed, Takemura and Yabe [54] investigated on the dissolution rate of a carbon dioxide contaminated bubble with experiments and simulations for $Re < 100$ and observed a transfer rate decrease until the same rate as for a solid sphere. Then, the authors introduced the reduced Sherwood number $Sh^*$ defined from the values predicted for a clean bubble and for a solid sphere. They estimated $Sh^*$ by a function of $C_D^*$, without taking into account any other effect of the Schmidt number apart from the contribution in the predictions used for the normalization. This transfer decrease was also analyzed in the exper-

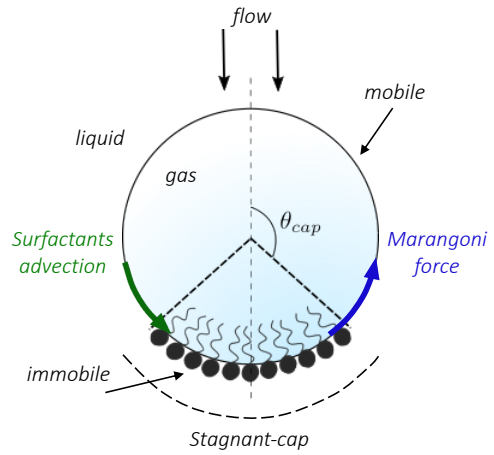


**Figure 1:** Schematization of the stagnant-cap regime for a spherical rising bubble in a quiescent liquid. Adsorbed surfactants are advected to the bubble rear where they form a constant stagnant-cap angle $\theta_{cap}$ in steady state.

imental study of Vasconcelos et al. [61], where the mass transfer rate was observed to follow two contrasted regimes by measuring the dissolution of single bubbles: depending on the contamination level of the liquid, the mass transfer is found to be consistent with predictions of a clean bubble or to that of a solid sphere, with a sharp decrease reported between these two limits. To quantify this decrease, Painmanakul et al. [41] proposed a correlation which predicts the Sherwood number with a weighting given to the Sherwood number of a clean bubble and a solid sphere depending on the rate of surface covered by surfactants, the latter parameter being calculated from the Langmuir adsorption isotherm for soluble surfactants. Another study was performed by Dani et al. [13, 14] by means of direct numerical simulations: the stagnant-cap regime was assumed, by directly imposing the contamination angle and splitting the bubble surface into a mobile and immobile interface, thus the resolution of the surfactant transport equation coupled to the Marangoni stress was not required in their numerical method. They showed that while the Sherwood number depends on all the parameters $Re$, $Sc$ and $\theta_{cap}$, the values of $Sh^*$ are found to lie between an upper limit defined by the $C_D^*$ function of $\theta_{cap}$ from [49] in the creeping flow regime only (whatever $Sc$), and a lower limit defined by another function of $C_D^*$ provided that both the Reynolds and Schmidt numbers are large; however, for intermediates values of these paremeters, the points are dispersed between these two limits. Recent experimental investigation with Planar Laser Inhibition induced by Fluorescence (PLIF, [63]) was carried out by Jimenez et al. [24] to evaluate the mass transfer from oxygen bubbles in demineralized water, water contaminated by surfactants and filtered water extracted from a sewage plant, therefore in liquid phases with impurities or surfactant concentrations above the critical micellar concentration. The authors also observed a significant decrease of the mass transfer rate while the liquid side diffusion coefficient remained unchanged. Similar results were observed by Lebrun and al. [30], including the case of liquids of complex rheology. A relevant comparison between experimental results from Madhavi et al. [35] and the numerical model of Jia and Zhang, which takes into account bubble shrinkage during dissolution and contaminants accumulation based on the stagnant-cap approach, was carried out on the bubble size evolution in [23]. However, there exists no general correlation on the Sherwood number able to quantify the gradual transfer decrease from that around clean bubbles towards that around solid spheres [1] depending on the coverage rate of the interface.

In this paper, direct numerical simulations of the hydrodynamics and mass transfer around a spherical rising bubble, contaminated by insoluble surfactants, are considered. The latter are already adsorbed at the interface, convected along the bubble surface at a rate which is much higher than that of both surface diffusion and adsorption-desorption, which makes strong surface concentration gradients and Marangoni effect to develop, resulting in the stagnant-cap regime. With this numerical approach, the contamination angle is not imposed but is a result of the simulation model, like in [18, 44] and unlike most of the previous numerical studies with mass transfer around contaminated bubbles [13, 14, 55, 23]. Once the steady state for the hydrodynamics is reached, the mass transfer dynamics (physical absorption) of a solute from the gas to the liquid phase is computed, by assuming a slight rate of mass transfer so that the change of the bubble volume can be neglected. The aim of this study is to quantify the impact of the different parameters (Reynolds number, contamination angle, Schmidt number) on the bubble dynamics and the Sherwood number. As there is no existing general correlation describing the external mass transfer rate in the presence of surfactants, the main motivation of the present work is to provide a complete model taking into account the relevant parameters, from a clean to a fully contaminated bubble.

## 2. Physical model and numerical methods

In this section, details are provided about the mathematical formalism used to describe the physical phenomenon. The direct numerical simulations were performed with the in-house code DIVA (Dynamics of Interfaces for Vaporization and Atomization) based on the Level-Set and Ghost Fluid methods, of which the numerical methods are detailed in 2.2.

### 2.1. Governing equations

Incompressible two-phase flows are simulated with the momentum and the mass conservation by solving the Navier-Stokes equations in a one-fluid approach,

$$\rho\left(\frac{D\vec{u}}{Dt} + (\vec{u}\cdot\vec{\nabla})\,\vec{u}\right) = -\nabla p + \nabla.(2\mu\bar{\bar{D}}) + \rho\vec{g} \ , \qquad (1)$$

$$\nabla\cdot\vec{u} = 0 \ , \qquad (2)$$

where $\rho$ and $\mu$ are respectively the fluid density and viscosity, $\vec{u}$ the velocity field, $p$ the pressure, $\bar{\bar{D}}$ the rate of deformation tensor, $\vec{g}$ the gravity acceleration. Across the interface, the following jump condition on the normal stresses due to capillary effects is satisfied,

$$[\vec{n} \cdot (-p\bar{\bar{I}} + 2\mu\bar{\bar{D}}) \cdot \vec{n}] = \sigma\kappa \ , \tag{3}$$

where [.] is the interface jump condition operator defined as $[A] = A_{liq} - A_{gas}$ for a field $A$, $\sigma$ the surface tension, $\kappa = -\nabla.\vec{n}$ the interface curvature with $\vec{n}$ the normal vector to the interface. Here, the phase change induced by mass transfer is not considered, therefore the normal velocity is continuous across the interface, as well as the tangential velocity (no interfacial slip between the two phases), leading to,

$$[\vec{u}] = \vec{0} \ . \tag{4}$$

In the absence of surfactant exchanges from or to the bulk phase, the initially adsorbed surfactants are advected along the bubble surface following a surface advection-diffusion equation [33, 50],

$$\frac{\partial\Gamma}{\partial t} + \nabla_s \cdot \left(\Gamma\vec{u}\right) = D_s \Delta_s\Gamma \ , \tag{5}$$

where $\Gamma$ is the surface concentration of surfactants, $\nabla_s = \left(\bar{\bar{I}} - \vec{n}\otimes\vec{n}\right)\vec{\nabla}$ the surface gradient operator, $D_s$ the surface diffusion coefficient and $\Delta_s$ the surface laplacian operator. By developing the second term of eq.(5), the surfactant transport equation on the interface becomes,

$$\frac{\partial\Gamma}{\partial t} + u_s \cdot \nabla_s\Gamma + \Gamma\nabla_s \cdot \vec{u} = D_s \Delta_s\Gamma \ , \tag{6}$$

where $u_s$ is the tangential velocity. In eq.(6), note that the partial time derivative is taken along the normal to the interface. In this study, the surface diffusion term is neglected, by assuming an infinite surface Péclet number for the surfactant transport. Note that this is a reasonable hypothesis based on typical values of the surface diffusion coefficient [60]. Surface advection leads to a non-uniform $\Gamma$ profile along the interface, which triggers gradients of surface tension and resulting Marangoni interfacial stresses, mathematically described as a jump condition of the tangential viscous stresses across the interface,

$$\left[\mu\left(\frac{\partial u_s}{\partial n} + \frac{\partial u_n}{\partial s}\right)\right] = \nabla_s\sigma \ . \tag{7}$$

Note that, in the frame moving with the bubble, the normal velocity $u_n$ is zero (and is continuous) along the whole surface of the spherical bubble, leading to $\frac{\partial u_n}{\partial s} = 0$. The surface tension $\sigma$ locally varies depending on the surfactant concentration,

$$\sigma = \sigma_0 - R_g T\Gamma \ , \tag{8}$$

where $\sigma_0$ is the surface tension in a clean configuration, $R_g$ the gas constant and $T$ the temperature which remains constant in this study. Note that eq. (8) is only valid in dilute surface concentration of surfactants, i.e. far from the packing.

In a gas-liquid configuration, the resistance to mass transfer mainly lies in the liquid phase where the diffusion is much slower than in the gas phase, therefore only the liquid side is considered in this study by computing the advection-diffusion equation for the concentration $C$ of a single species of dissolved gas,

$$\frac{\partial C}{\partial t} + \vec{u} \cdot \nabla\vec{C} = D \ \nabla \cdot (\nabla\vec{C}) \ , \tag{9}$$

where $D$ is the diffusion coefficient associated to the solute-liquid binary mixture. In this study, the system of eq. (1), (2), (6), (9) are computed until steady-state in the frame moving with the bubble, with their respective jump and boundary conditions.

## 2.2. Numerical methods

The above equations are implemented in the in-house code DIVA [57, 58, 29, 46, 32] which has been extensively validated by theoretical, experimental and numerical comparisons for various studies including the dynamics of shape oscillations of rising bubbles [26] and droplets in the presence of surfactants [45], fluids-membrane interaction [12] where a similar numerical approach was used to impose a jump condition on the tangential stresses across the interface, mass transfer in the presence of phase change phenomena [39, 47, 59] or within gas-liquid Taylor flows [8].

The Level-Set method [40] is used to compute the interface motion by solving a convection equation for a distance-function $\phi$ of which positive and negative values correspond respectively to liquid and gas field,

$$\frac{\partial\phi}{\partial t} + \vec{u} \cdot \nabla\phi = 0 \ . \tag{10}$$

A reinitialization step as proposed in [51] is used to maintain $\phi$ as a signed distance function, at each time step.

A sharp implementation for the jump conditions at the interface is carried out with the Ghost Fluid method [16], which consists in extrapolating the discontinuous variables across the interface by computing ghost values in order to enforce an accurate discretization of the derivatives near the interface. The Navier-Stokes incompressible equations (1) are solved with a projection method where the pressure and viscous discontinuities are taken into account with the Ghost Fluid Conservative viscous Method (GFCM) detailed in [29], in an implicit formulation as mentioned in [32]. The Poisson equation resulting from this projection step is solved by a BlackBox MultiGrid (BBMG) solver [15] which ensures a fast and stable resolution. The convective terms of equations (1), (9) and (6) are computed with a fifth order Weighted Essentially Non-Oscillatory (WENO-Z) schemes [4], the temporal derivatives with a second order Runge-Kutta schemes and other spatial derivatives with second order finite difference schemes.

The surfactant concentration $\Gamma$ field is extended to both sides of the interface by a constant extrapolation in the nor-

mal direction [2] as suggested in [64],

$$\frac{\partial \widetilde{\Gamma}}{\partial \tau} + sign(\phi)\vec{n}\cdot\vec{\nabla}\widetilde{\Gamma} = 0 \ , \tag{11}$$

in order to remove the normal derivative:

$$\vec{n}\cdot\vec{\nabla}\widetilde{\Gamma} = 0 \ , \tag{12}$$

where $\widetilde{\Gamma}$ is the extrapolated surfactant concentration field and $\tau$ a fictitious time required to obtain the condition given by eq.(12). Therefore, $\nabla_s\Gamma = \nabla\widetilde{\Gamma}$ is satisfied, which enables the resolution of eq. (6) on a mesh grid which is not boundary-fitted. Besides, the use of the extended $\widetilde{\Gamma}$ field allows to compute the time derivative in eq.(6) as the usual Eulerian one at a fixed point of space, as explained in [43]. Benchmarks for a validation of this equation implementation have been performed in [45].

A sharp methodology has been used to take into account the Marangoni jump condition on the tangential viscous stresses in the Navier-Stokes equations. For a 2D example, the viscous term of (1) gives,

$$\nabla.(2\mu\bar{\bar{D}}) = \begin{pmatrix} \frac{\partial}{\partial x}\left(2\mu\frac{\partial u}{\partial x}\right) + \frac{\partial}{\partial y}\left(\mu\left(\frac{\partial u}{\partial y} + \frac{\partial v}{\partial x}\right)\right) \\ \frac{\partial}{\partial x}\left(\mu\left(\frac{\partial u}{\partial y} + \frac{\partial v}{\partial x}\right)\right) + \frac{\partial}{\partial y}\left(2\mu\frac{\partial v}{\partial y}\right) \end{pmatrix} \ , \tag{13}$$

in which the jump condition from eq.(7) is imposed in the cells crossed by the interface following the methodology of [25] such as,

$$\left[\mu\frac{\partial u}{\partial x}\right] = n_x\,\nabla_s\sigma \ , \quad \left[\mu\frac{\partial u}{\partial y}\right] = n_y\,\nabla_s\sigma \ , \tag{14}$$

$$\left[\mu\frac{\partial v}{\partial x}\right] = n_x\,\nabla_s\sigma \ , \quad \left[\mu\frac{\partial v}{\partial y}\right] = n_y\,\nabla_s\sigma \ . \tag{15}$$

These jump conditions are added in the projection step of the resolution by the GFCM method. Validation and details about this implementation can be found in [12].

Concerning mass transfer of the solute, a Dirichlet boundary condition is imposed at the immersed interface to set the solute concentration to a value of $C_{int}$. Here, it is assumed that $C_{int}$ remains constant (as predicted by the standard Henry law), considering therefore that the mass transfer decrease is only due to a modification of the hydrodynamics in these simulations, and that there is no additional mass transfer barrier at the interface due to the presence of adsorbed surfactants (note that a more sophisticated modelling including hindrance effect [5] could be achieved by modifying this boundary condition). In the present computations, the immersed Dirichlet condition at the interface is achieved by using the second order numerical scheme proposed in [20]. Moreover, for an accurate calculation of the concentration gradients at the interface and their transport, quadratic extrapolations are used to build extensions of the liquid phase concentration inside the gas by ensuring the continuity of the concentration profile and of its first and second normal derivatives at the interface, as proposed in [2].

| $Ar$ | $Ma$ | $Re$ | $\theta_{cap}$ |
|---|---|---|---|
| $4.28.10^2$ | 0 | 19.7 | $\pi$ |
| $4.28.10^2$ | 0.1 | 18.5 | 2.34 |
| $4.28.10^2$ | 0.3 | 15.0 | 1.97 |
| $4.28.10^2$ | 0.5 | 13.7 | 1.73 |
| $4.28.10^2$ | 0.7 | 13.0 | 1.49 |
| $4.28.10^2$ | 1 | 12.2 | 1.22 |
| $4.28.10^2$ | 2 | 11.6 | 0.35 |
| $4.28.10^2$ | 3 | 11.6 | 0 |
| $1.57.10^3$ | 0 | 57.6 | $\pi$ |
| $1.57.10^3$ | 0.1 | 56.0 | 2.42 |
| $1.57.10^3$ | 0.3 | 44.2 | 2.08 |
| $1.57.10^3$ | 0.5 | 38.5 | 1.87 |
| $1.57.10^3$ | 0.7 | 35.8 | 1.64 |
| $1.57.10^3$ | 1 | 33.4 | 1.39 |
| $1.57.10^3$ | 2 | 30.1 | 0.77 |
| $1.57.10^3$ | 20 | 29.6 | 0 |
| $2.81.10^3$ | 0 | 94.5 | $\pi$ |
| $2.81.10^3$ | 0.1 | 97.5 | 2.42 |
| $2.81.10^3$ | 0.3 | 68.6 | 2.13 |
| $2.81.10^3$ | 0.5 | 57.8 | 1.91 |
| $2.81.10^3$ | 0.7 | 53.5 | 1.65 |
| $2.81.10^3$ | 1 | 50.5 | 1.40 |

**Table 1**
Hydrodynamics conditions and results for a contaminated bubble. At each ($Ar$, $Ma$), the Reynolds number $Re$ and the contamination angle $\theta_{cap}$ are obtained from the numerical resolution.

## 3. Results

Simulations are performed in a 2D axisymmetric coordinate configuration with a non-uniform Cartesian mesh. The bubble of radius $R$ is maintained at the center of the domain of size $l_r \times l_z = 8R \times 16R$ to avoid containment effects, in a moving frame by using a method similar to [37]. For the velocity field, symmetric and wall conditions are respectively imposed at $r = 0$ and $r = l_r$, and free boundary conditions are imposed at the top and bottom boundaries. The following boundary conditions are imposed for the mass field: a Dirichlet condition $C_{int} = 1\,\mathrm{mol.m^{-3}}$ at the bubble surface, a Neumann condition with a zero flux at $r = 0$ and Dirichlet conditions with $C_\infty = 0$ at $r = l_r$, $z = 0$ and $z = l_z$. First, the hydrodynamics of the rising bubble in the presence of the adsorbed surfactants is computed until steady-state. Then, mass transfer is solved based on the converged velocity field.

Concerning the hydrodynamics, simulations are carried out at constant density and viscosity ratios respectively of values 815 and 63, corresponding to the case of a bubble immersed in a liquid, at three different values of the Archimedes numbers $Ar$ which fixes the ratio between gravitational and viscous forces. For a given $Ar$, simulations are performed at different Marangoni numbers $Ma$, which compare the intensity of the stress due to the Marangoni effect to the viscous shear stress, and is varied in the range $Ma = 0{-}20$ by changing the average surfactant concentration at the interface $\overline{\Gamma}$ to consider cases between that of a fully mobile to a fully im-

mobile interface. Therefore, at a given $Ar$, increasing $Ma$ leads to a decrease of the Reynolds number $Re$ based on the bubble rising velocity, its values lying between 11 and 100 in this study (data are provided in table 1). In addition, the Weber $We$ number, which compares the inertial stress tending to deform the bubble over the average surface tension, is maintained to a very small value ($We < 0.01$) in all simulations, which ensures that the bubble shape is spherical. All these dimensionless parameters are defined by

$$Ar = \frac{g\, d^3\, \rho_{liq}\left(\rho_{liq} - \rho_{gas}\right)}{\mu_{liq}^2} \;, \quad Re = \frac{\rho_{liq} U_\infty d}{\mu_{liq}} \;, \tag{16}$$

$$We = \frac{\rho_{liq} U_\infty^2 d}{\overline{\sigma}} \;, \qquad Ma = \frac{R_G T \overline{\Gamma}}{\mu_{liq} U} \;, \tag{17}$$

where $d$ the bubble diameter, $\rho_{liq}$ and $\rho_{gas}$ are respectively the liquid and gas densities, $\mu_{liq}$ the liquid dynamic viscosity, $U_\infty$ the rising terminal velocity, $\overline{\sigma}$ is the average surface tension calculated from eq.(8), $\overline{\Gamma}$ the average surfactant concentration at the interface, $R_G = 8.314\,\mathrm{J.K^{-1}.mol^{-1}}$ the ideal gas constant and $T$ the temperature set to $T = 293.15\mathrm{K}$. Note that $Ma$ has been defined by using the bubble velocity $U$ corresponding to the clean bubble case ($\overline{\Gamma} = 0$) at same $Ar$, since it is set before running the simulations with surfactants for which $U_\infty$ is not *a priori* known. For each couple ($Ar$, $Ma$), once the hydrodynamics steady state is reached, the angle of contamination $\theta_{cap}$ is measured from the surfactant concentration profile along the bubble surface as displayed in figure 2, as well as the corresponding Reynolds number related to the terminal rising velocity. In this way, the relevance of this approach lies in the free parameters $\theta_{cap}$ and $Re$ which are direct results from the complete numerical resolution which couples the hydrodynamics with the Marangoni stresses.

Once the hydrodynamics steady state is reached, the mass transfer is solved for different Schmidt numbers from $Sc = 5$ to $Sc = 70$, which induces a Péclet number $Pe$ range of $50 - 7000$,

$$Pe = \frac{U_\infty d}{D} \;, \qquad Sc = \frac{\mu_{liq}}{\rho_{liq} D} \;. \tag{18}$$

### 3.1. Effects of surfactants on the hydrodynamics

Regarding the stagnant-cap regime, when the steady state is reached, the advection term of equation eq.(5) is equal to zero and the following relation is obtained,

$$u_s\, \Gamma \;=\; 0 \;, \tag{19}$$

with $u_s$ the tangential velocity at the interface. Surface profiles of surfactant concentration and tangential velocity obtained by simulation are plotted in figure 2 at $Ar = 4.28 \cdot 10^2$ and $Ma = 0.3$. The front part is free of surfactants and the interface velocity is non-zero, until $\theta \approx 2.0$ which is the contamination angle for this case where a strong surface gradient of concentration and tangential velocity appears. At the rear ($\theta > 2.0$), the interface is immobile and the surfactant concentration is non-zero. This result is in good agreement with the theoretical condition expressed in eq.(19) and demonstrates an accurate capture of the strong gradients around $\theta_{cap}$. Moreover, a satisfactory spatial convergence is obtained in table 2 for the contamination angle when changing the mesh size.

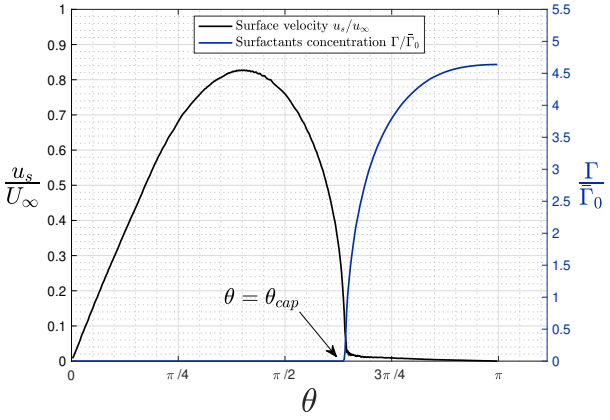


**Figure 2:** Surfactant concentration and tangential velocity at the bubble surface at $Ar = 4.28 \cdot 10^2$ and $Ma = 0.3$, corresponding to $Re = 15.04$.

The drag force between the liquid and the bubble is calculated from the following expression,

$$\vec{F}_D = \oint_S -p\overline{\overline{I}} \cdot \vec{n}\, \mathrm{d}S \;+\; \oint_S 2\mu \overline{\overline{D}} \cdot \vec{n}\, \mathrm{d}S \;, \tag{20}$$

where the former integral corresponds to the pressure drag force and the latter one to the viscous drag force, and the drag coefficient is finally obtained,

$$C_D = \frac{\|\vec{F}_D\|}{\frac{1}{2}\left(\pi R^2\right) \rho_{liq}\, U_\infty^2} \;. \tag{21}$$

Drag coefficients of bubbles with fully mobile (clean case) and fully immobile (solid-like case in terms of hydrodynamics) are respectively compared to the correlation of Mei et al. [36],

$$C_D^{clean} = \frac{16}{Re}\left[1 + \left(\frac{8}{Re} + \frac{1}{2}\left(1 + \frac{3.315}{Re^{1/2}}\right)\right)^{-1}\right] \;, \tag{22}$$

and Clift et al. [9],

$$C_D^{solid} = \frac{24}{Re}\left(0.1935\, Re^{0.6305}\right) \;. \tag{23}$$

Sadhal and Johnson [49] introduced a reduced drag coefficient to quantify the impact of surfactants on the hydrodynamics,

$$C_D^{*} = \frac{C_D \;\; - C_D^{clean}}{C_D^{solid} - C_D^{clean}} \;, \tag{24}$$

| | | Meshes | | | References | |
|---|---|---|---|---|---|---|
| | | $256 \times 512$ | $512 \times 1024$ | $1024 \times 2048$ | $C_D^{clean}$ | $C_D^{solid}$ |
| Clean bubble ($Re = 20$) | $C_D$ | 1.44 | 1.45 | 1.42 | 1.44 | - |
| Fully contaminated bubble ($Re = 11.6$) | $C_D$ | 4.16 | 4.09 | 4.05 | - | 3.97 |
| Partially contaminated bubble ($Re = 13.7$) | $C_D$ | 2.92 | 2.91 | 2.89 | - | - |
| Partially contaminated bubble ($Re = 13.7$) | $\theta_{cap}$ | 1.70 | 1.73 | 1.73 | - | - |

**Table 2**
Spatial convergence of the drag coefficient for a clean and a fully covered (with fully immobile interface) bubble at $Ar = 4.28 \cdot 10^2$, compared respectively to the correlation eq.(22) of Mei et al. [36] for a clean bubble and the correlation eq.(23) of Clift et al. [9] for a solid sphere. Spatial convergence of the drag coefficient and the contamination angle of a partially contaminated bubble, at same $Ar$ and $Ma = 0.5$.

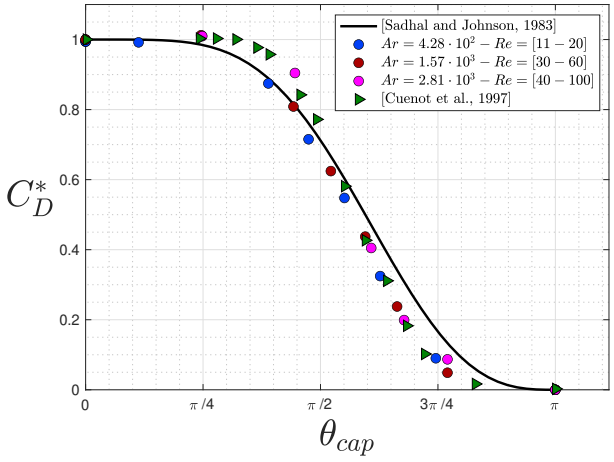


**Figure 3:** Comparison between reduced drag coefficients from this study to the correlation proposed by Sadhal and Johnson [49], at different Archimedes and Marangoni numbers.

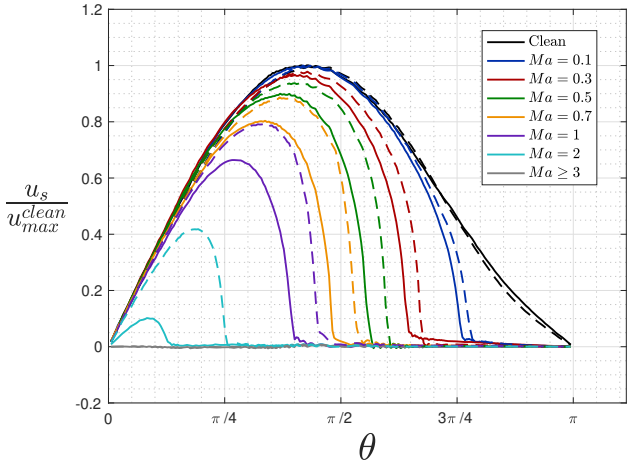


**Figure 4:** Dimensionless velocity profiles along the bubble surface at two different Archimedes numbers and at different Marangoni numbers for each of them. $-$ : $Ar = 4.28 \cdot 10^2$, $--$ : $Ar = 1.57 \cdot 10^3$.

and proposed the following analytical relation, under creeping flow conditions, between $C_D^*$ and the contamination angle for intermediate cases in terms of interface mobility,

$$C_{D-SJ}^* = \frac{1}{2\pi}\left[2(\pi - \theta_{cap}) + sin(\theta_{cap}) + sin(2\theta_{cap}) - \frac{1}{3}sin(3\theta_{cap})\right] , \quad (25)$$

It has previously been shown that drag coefficients of bubbles at large Reynolds numbers fit also to this correlation [11, 55], with slight discrepancies due to the different hydrodynamic conditions. Drag coefficients obtained in this study at different Marangoni numbers are plotted in fig. 3, and are also in good agreement with eq. (25). Numerical details about the spatial convergence of our results can be found in table 2. Note that figure 3 shows that a drag coefficient equal to that of a solid sphere can be reached even if the interface is not fully immobile, provided that $\theta_{cap} < \pi/3$, as observed in [45] in the case of contaminated liquid droplets.

In this work, a further analysis of the impact of surfactants on the local hydrodynamics is proposed, hereafter. For this purpose, tangential velocity profiles along the interface are plotted in fig. 4 for different couples ($Ar$, $Ma$). The velocities $u_s$ are made dimensionless with the maximum velocity at the bubble surface for a clean bubble, which depends only on $Re$ as shown in [31],

$$u_{max}^{clean} = \frac{1}{2}\frac{16 + 3.315Re^{0.5} + 3Re}{16 + 3.315Re^{0.5} + Re}U_\infty \ . \quad (26)$$

Fig. 4 shows that, for a clean bubble, the maximal value of the normalized $u_s$, denoted as $u_{s\,max}$, is in perfect agreement to 1, and decreases depending on the degree of the interface contamination: the larger the portion of immobile interface (i.e the higher the coverage rate), the smaller the maximum interface velocity. In particular, the normalization by $u_{max}^{clean}$ permits to remove the dependency on $Re$, which varies significantly between the different presented cases from 11 to 60. Thus, the ratio $u_{max}^* = u_{s\,max}/u_{max}^{clean}$ is a function of $\theta_{cap}$ only. It can be noted that the velocity decrease from the clean profile is smooth for $\theta_{cap} > 1.5$ while it is stronger at larger coverage rates.To quantify this local aspect, for all our simulation points in the range $10 < Re < 100$, the values of $u_{max}^*$ are plotted as a function of $\theta_{cap}$ in fig. 5 by including other data from [11] and [14]. A master curve which gathers

all these results is noticeable, whatever the $Ar$, $Re$ and $Ma$ values in this range. Hence, the following fitting function is proposed to predict this dimensionless maximum velocity, which varies between 0 and 1:

$$u^*_{max} = 0.5216 \tanh(1.8\ \theta_{cap}^{0.85} - \pi/2) + 0.4784 \quad (27)$$

It is confirmed that $u^*_{max}$ does not change in the region of small contamination ($\theta_{cap} \geq 3\pi/4$) while it significantly varies for $\theta_{cap} \leq \pi/4$ when the coverage rate of the interface is high, despite the fact that the drag coefficient is already that of a solid sphere in this region. The scaling of $u^*_{max}$ will be further used in this paper to predict the Sherwood number around contaminated bubbles.

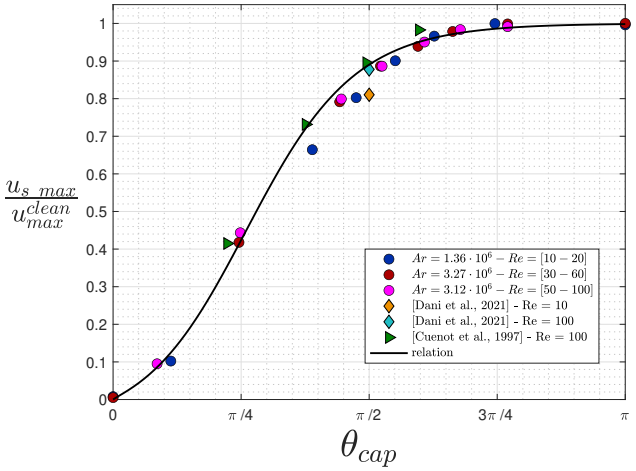


**Figure 5:** Evolution of the maximal velocity $u^*_{max}$ at the bubble surface at different contamination angles.

The only required parameter to compute $u^*_{max}$ is the contamination angle, which is plotted in fig. 6 as a combined function of both the Reynolds number and the Marangoni numbers (the latter being defined based on $U_\infty$ for this plot). It can be seen that the latter gathers all our simulation points, for Reynolds numbers between 10 and 100. It shows that $\theta_{cap}$ is mainly given by the $Ma$ parameter, but also involves a correction due to inertial effects through $Re$.

Such a master curve reveals that, in the range of the investigated parameters, when the interface is fully immobile ($\theta_{cap} = 0$), there exists a threshold value of $Ma^{1.55}/Re^{0.6}$ for which a further increase of $Ma$ (by increasing $\overline{\Gamma}$ for example) has no impact on the hydrodynamics anymore. This is consistent with the experimental results of Bel Fdhila et al. [3] and Jimenez et al. [24] where the bubble rising velocity was found to be independent of the (bulk) surfactant concentration after a given value. In an experimental configuration, by measuring $U_\infty$ and deducing $\theta_{cap}$ (from fig. 3), the plot of fig. 6 can provide an estimate of the average surface concentration of surfactants at the interface, which is a quantity involved in $Ma$ and difficult to measure.

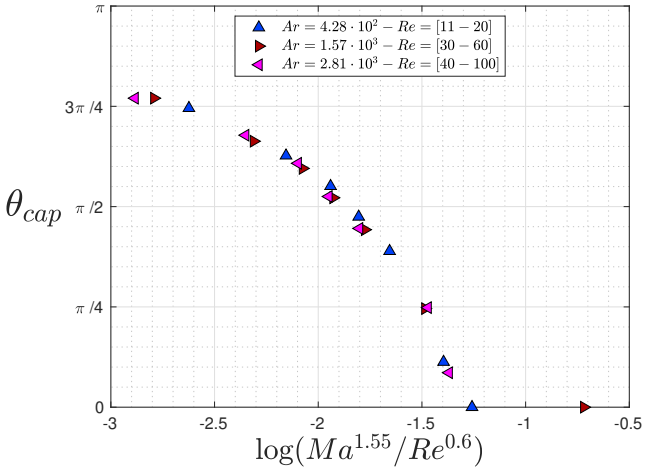


**Figure 6:** Evolution of the stagnant-cap angle as a function of the Marangoni and Reynolds numbers, at three different Archimedes numbers. In this figure, $Ma$ is defined on the rising velocity reached in the steady-state of the contaminated bubble.

## 3.2. Effects of surfactants on mass transfer: investigation on the Sherwood number

In this section, the mass transfer rate around the contaminated bubble is quantified. First, simulations for the clean configuration and the fully contaminated bubble are performed to validate the mass transfer solver and the size of the mesh required depending on the Péclet number value. Indeed, to capture thin mass boundary layers corresponding to high $Pe$, a very refined Cartesian mesh is required as illustrated in 1. After validation, a parametric study is carried out by varying $Sc$ for each contaminated bubble of table 1. Then, to evaluate the average mass flux, the Sherwood number $Sh$ is computed once it reaches a constant value, by the following surface integral,

$$Sh = \frac{d}{D\,(C_{int} - C_\infty)} \frac{1}{S} \iint_S -D\,\vec{\nabla}C \cdot \vec{n}\,\mathrm{d}S \ . \quad (28)$$

### 3.2.1. Mass transfer around a clean and a fully-contaminated bubble

The two extreme cases of mass transfer around a bubble with fully-mobile (clean bubble) or fully-immobile (solid-like case) interface are considered in this section, as they serve as reference cases for the intermediate regimes of contamination in the next section.

Concerning the case of a clean bubble, at large $Pe$ and $Re$, the mass transfer rate can be quantified by the potential flow solution of Boussinesq [7], which is the dimensionless form of the Higbie's penetration theory [21], showing that $Sh^{clean}$ tends towards $2/\sqrt{\pi}Pe^{1/2}$. Indeed, such a scaling can be found by balancing the characteristic time of advection $\tau_{adv} = d/U_c$ (defined by considering that the characteristic convection velocity $U_c \sim U_\infty$ is the tangential velocity of the fluid along the mobile interface, of order of the bubble

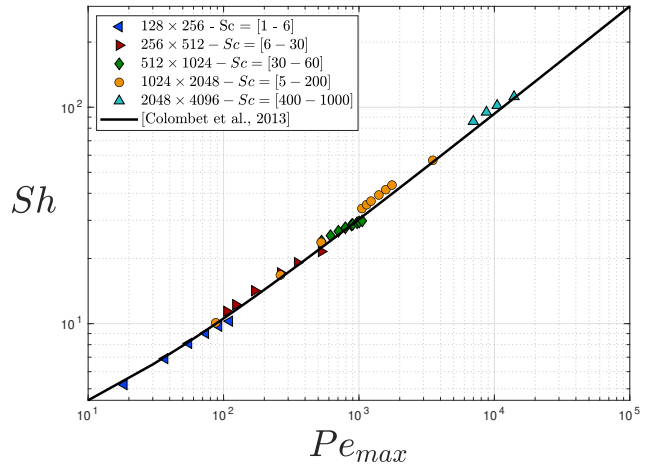


**Figure 7:** Comparison between the global Sherwood number obtained for a clean bubble at $Re = 20$ and the correlation (31) from [10].

rising velocity) and diffusion $\tau_{diff} = (\delta_m^{clean})^2/D$ within the mass boundary layer of thickness $\delta_m^{clean}$, which finally results in

$$Sh^{clean} \sim d/\delta^{clean} \sim Re^{1/2}Sc^{1/2} \tag{29}$$

from the film theory.

For intermediate values of $Pe$ and $Re$, the mass transfer around a clean bubble can be computed from the relation proposed by Takemura and Yabe [53], which includes an empirical correction of the Boussinesq solution, established from cases at $Re < 100$ and $Pe > 1$,

$$Sh_1^{clean} = \left(\frac{2}{\sqrt{\pi}}\right)\left[1 - \frac{2}{3}\frac{1}{(1+0.09Re^{2/3})^{0.75}}\right]^{0.5} \times (2.5 + Pe^{1/2}) \ . \tag{30}$$

Another correlation has been proposed by Colombet et al. [10] for a complete range of Reynolds and Péclet numbers,

$$Sh_2^{clean} = 1 + \left[1 + \left(\frac{4}{3\pi}\right)^{2/3}(2\,Pe_{max})^{2/3}\right]^{3/4} \ , \tag{31}$$

satisfying both the Boussinesq limit and the opposite limit in the pure diffusion case, and defined by using $Pe_{max}$ which is the Péclet number based on the maximum velocity at the bubble surface computed from eq. (26). According to the authors, the latter parameter is the most relevant one to describe external (or internal) mass transfer of a rising bubble in a stagnant liquid. Note that eq. (30) and (31) give very close prediction of $Sh_{clean}$, with a discrepancy below 5 %, even in a larger range of $Re$ than that given by Takemura and Yabe in their original article ($Sh_1^{clean}$ being always slightly smaller than $Sh_2^{clean}$).

Numerical results of this work are compared to the predictions of eq. (31) in fig. 7 for the simulations performed at $Re = 20$ and $Sc = [1 - 1000]$. A good agreement is obtained, with maximal differences of about 10 %. By increasing the Schmidt number, a thinner mesh is required to accurately capture the mass flux at the interface in direct numerical simulations (without introducing subgrid-scale models for mass transfer as in [6, 62]). The spatial convergence is shown in table 3, and our numerical results are observed to be properly converged provided the mass boundary layer is described by at least ten mesh cells.

| | $Sh$ for different meshes | | | References | |
|---|---|---|---|---|---|
| $Sc$ | 256 ×512 | 512 ×1024 | 1024 ×2048 | $Sh_1^{clean}$ | $Sh_2^{clean}$ |
| 30 | 24.1 | 23.8 | 22.7 | 22.5 | 22.4 |
| 60 | 29.8 | 34.0 | 34.5 | 30.9 | 31.1 |

**Table 3**
Spatial convergence on the Sherwood number at $\theta_{cap} = 0$ for $Sc = 30$ and $Sc = 60$, compared to the prediction of eq. (30) and (31) for a clean bubble.

Concerning mass transfer around a fully-contaminated bubble (i.e. with a fully-immobile interface), Takemura and Yabe [54] have shown that the corresponding Sherwood number is the same as for the case of a solid sphere. In this extreme case, $Sh^{solid}$ scales differently than $Sh^{clean}$. Indeed, the characteristic convection velocity for interfacial mass transfer scales in that case as $U_c = \frac{U_\infty \delta_m^{solid}}{\delta_h^{solid}}$ by considering that the velocity gradient $U_\infty/\delta_h^{solid}$ within the hydrodynamic boundary layer (of thickness $\delta_h^{solid} \sim d/\sqrt{Re}$) is exerted at the scale of the mass boundary layer of thickness $\delta_m^{solid}$. By equalizing the convection $d/U_c$ and diffusion time scales $(\delta_m^{solid})^2/D$, a scaling law of $\delta_m^{solid}$ can be obtained. By considering that $Sh^{solid} \sim d/\delta_m^{solid}$ from the film theory, it results that

$$Sh^{solid} \sim d/\delta_m^{solid} \sim Re^{1/2}Sc^{1/3} \ . \tag{32}$$

It can be noted, by comparing eq. (32) and eq. (29), that the exponent of the Schmidt number differs in between the case of a solid sphere compared to that of a clean bubble (whereas that of $Re$ is the same), explaining that the mass transfer rate is smaller in the former case at the same values of $Re$ and $Pe$, with a thicker average mass boundary layer around the bubble with fully immobile interface.
In this way, the Sherwood number around a fully-contaminated bubble can be described by the correlation of Clift et al. [9], obtained from numerical simulations,

$$Sh^{solid} = 1 + Re^{0.41}Sc^{1/3}\left(1 + \frac{1}{Pe}\right)^{1/3} \ , \tag{33}$$

to describe the transfer around a solid sphere at $Re \leq 400$ and $0.25 \leq Sc \leq 100$. Results from our simulations and the prediction of eq. (33) on $Sh^{solid}$ are compared in fig. 8, at two different $Re$ and several $Pe$ values until 1000. One can observe the very good agreement between the numerical

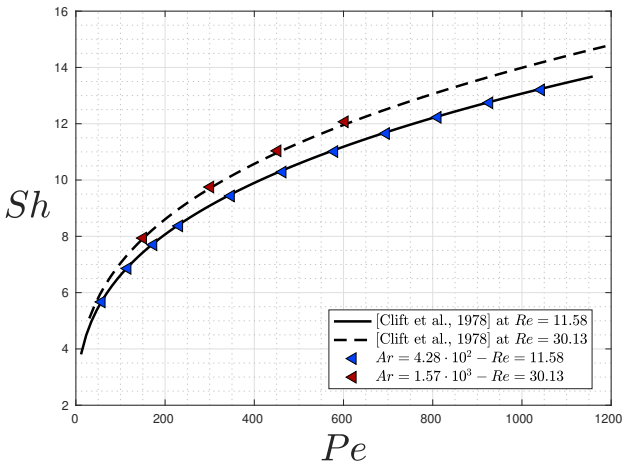


**Figure 8:** Comparison between the global Sherwood number obtained for a fully covered bubble (at $Re = 11.6$ and $Re = 30.1$) and the correlation (33) from [9], for $Sc < 100$.

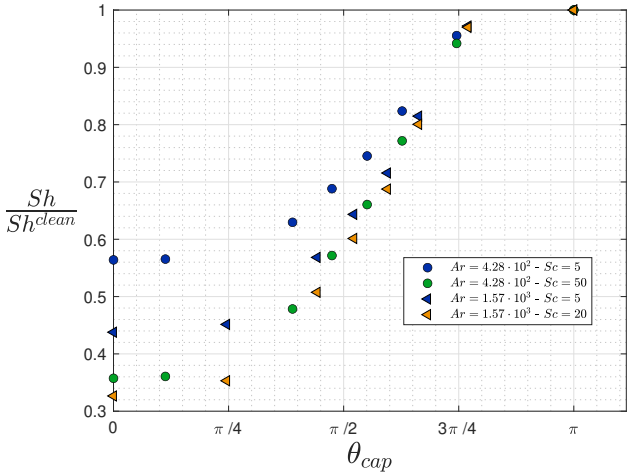


(a) Sherwood number depending on the contamination angle.

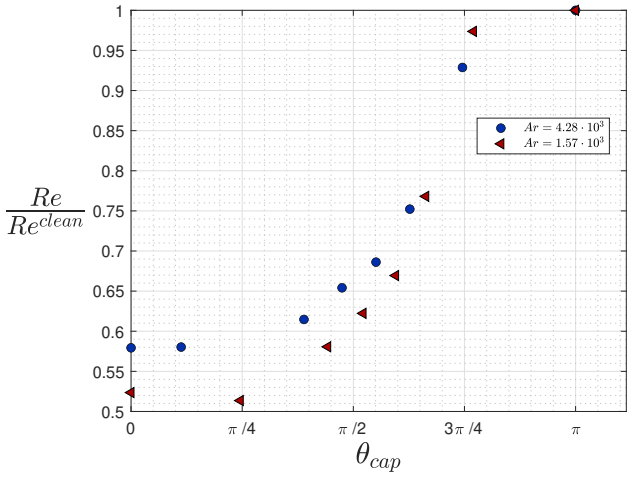


(b) Reynolds number depending on the contamination angle.

**Figure 9:** Sherwood and Reynolds numbers at $Ar = 4.28 \cdot 10^2$ and $Ar = 1.57 \cdot 10^3$. The reference values $Sh^{clean}$ and $Re^{clean}$ correspond to the values obtained for the case at same parameters (same $Ar$ and $Sc$ in particular) except that $Ma = 0$ (without surfactants).

simulations and eq.(33), the discrepancy being of approximately 0.4 %.

In the following section, the case of a partially contaminated bubble is addressed.

### *3.2.2. Global Sherwood number for a contaminated bubble*

A parametric study is carried out by varying the Schmidt number, at given values of the couple ($Ar$, $Ma$). From the validation tests, the range $Sc = [5 - 70]$ has been chosen in order to satisfy the mesh criteria permitting an accurate computation of $Sh$ (the corresponding meshes have ten points in the mass boundary layer, for a total of about one million points in the whole domain).

For two different values of $Ar$, fig. 9a and 9b plots the evolution of both the Sherwood and the Reynolds numbers when increasing $Ma$ i.e. the degree of contamination of the interface from the fully-mobile to the fully-immobile condition, as a function of the resulting $\theta_{cap}$. Both $Re$ and $Sh$ are divided by the value related to the clean case defined as the case at same $Ar$ and $Ma = 0$, in order to highlight the deviation of the mass transfer from the reference of the clean bubble. At a given $Ar$, such numerical experiments correspond to experimental conditions describing a bubble of same physical parameters except its surface concentration of adsorbed surfactants. In that case, it can be seen that $Re$ is divided approximately by a factor 2 in between the two extreme interface mobility conditions. Moreover, at a given $Sc$, $Sh$ decreases when increasing $Ma$ (thus decreasing $\theta_{cap}$) from the clean to the fully-contaminated bubble case, a strong correlation being noticed between the decrease of the ratios $Sh/Sh_{clean}$ and $Re/Re_{clean}$. However, $Sh/Sh_{clean}$ can be divided by a factor larger than 2, and the higher $Sc$, the higher this reduction factor. The influence of $Sc$ needs to be understood by analyzing the $Sh$ values at same $Re$.

For this purpose, the global Sherwood numbers at $Ar = 4.28 \cdot 10^2$ are plotted on fig. 10, $Re$ being the same for the points at same $\theta_{cap}$ (on vertical lines).

Under this condition of same $Re$, it clearly appears that $Sh$ does not always follow the same function of $Sc$. Indeed, at $\theta_{cap} = \pi$ (clean case), when $Sc$ is increased from 5 to 70 (multiplied by 14), $Sh$ is increased by a factor $3.7 = 14^{1/2}$; at $\theta_{cap} = 1.5$, $Sh$ is increased by a factor 2.9 and at $\theta_{cap} = 0$ (solid-like case) the factor is of $2.3 \approx 14^{1/3}$ . Thus, when a bubble is covered by surfactants, another effect than the Reynolds number decrease due to the partial immobilization of the interface explains the decrease of $Sh$: at a given $Re$, the influence of $Sc$ depends on $\theta_{cap}$. Indeed, the rate of variation of $Sh$ as a function of $Sc$ lies between the two limits

of $Sc^{1/2}$, as for a clean bubble, and $Sc^{1/3}$, as for a solid sphere, as shown in the previous section, by monotonously decreasing in between as evidenced here.

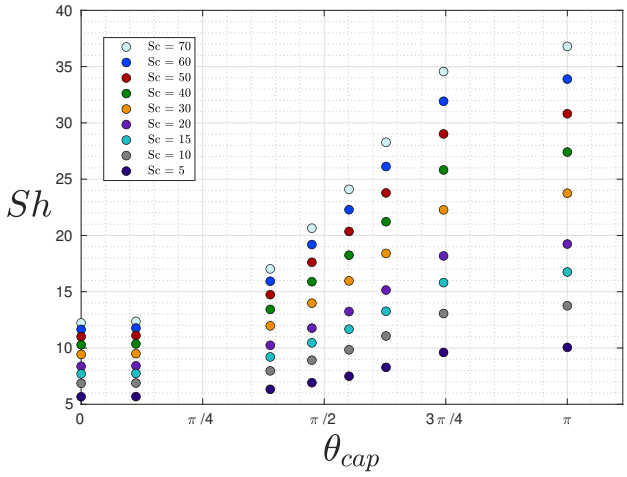


**Figure 10:** Global Sherwood number at $Ar = 4.28 \cdot 10^2$ for each simulation of $(Ar, Ma)$, at different Schmidt numbers (each point corresponds to a simulation). The Reynolds number corresponding to these simulations varies in the range $[11-20]$.

The different behaviours in terms of $Sc$, induced by the partial immobilization of the interface, can be spatially observed on the concentration fields. At $Ar = 4.28 \cdot 10^2$, the dimensionless solute concentration in the liquid phase, dimensionless surfactant concentration on the bubble surface and velocity fields are plotted at $Sc = 40$ in fig. 11, for $Ma = 0.3$ on the left, $Ma = 0.7$ in the middle and $Ma = 2$ on the right. For each case, based on the concentration fields, at the angular position corresponding to $\theta_{cap}$, one can observe a singularity of the boundary layer thickness along the interface which suddenly becomes thicker for $\theta \geq \theta_{cap}$, i.e. at the rear part where the interface velocity drops to zero. The average thickness of the mass boundary layer of a partially contaminated bubble therefore lies between the two extreme cases of clean bubble and solid sphere, in consistency with the variation of the exponent of $Sc$ in $Sh$. However, whatever the contamination angle, it is noted in fig. 11 that the mass boundary layer is always thinnest at the front part of the bubble, resulting that it is the location where the maximum part of the transfer takes place around the bubble, similarly to the case of clean bubbles [10, 17].

### *3.2.3. Profiles of local mass flux*

The distribution of the local mass flux is analyzed, by plotting the profiles of the local Sherwood number,

$$Sh_{loc} = \frac{-d\,\vec{\nabla}C \cdot \vec{n}}{(C_{int} - C_{\infty})}\ , \tag{34}$$

around the interface in fig. 12, for the case at constant $Sc = 70$ and $Ar = 4.28 \cdot 10^2$ but at different Marangoni numbers (thus at different $Re$). In the part free of surfactants, the mass flux follows the profile of the clean bubble but with a lower intensity than for the fully mobile case. It is confirmed that the main part of the transfer is always due to the front part of the bubble. Then $Sh_{loc}$ drops around $\theta_{cap}$ and follows a different evolution for $\theta > \theta_{cap}$. Indeed, the local flux profile presents a singularity around $\theta_{cap}$ as a consequence of the transition of the mass boundary layer thickness depending on the local interface mobility, as it was also mentioned in [23].

One can notice that the local mass flux profiles are different at $Ma = 2$ and $Ma = 3$, whereas (i) the $Re$ of both cases is the same (equal to the one of a solid sphere as shown in figure 3) and (ii) the evolution as $Sc$ already corresponds to an evolution as $Sc^{1/3}$ from the analysis of the corresponding points (at the two smallest $\theta_{cap}$ values) in fig. 10. However, the local hydrodynamics is different between these two cases, as shown by the tangential velocity profiles at the interface given in fig. 4: the case at $Ma = 2$ still presents a mobile zone along its interface ($\theta_{cap} = 0.35$), with a maximal velocity strongly reduced ($u^*_{max} = 0.1$) compared to what it would be at same $Re$ for a clean bubble based on fig. 5, whereas at $Ma = 3$ the interface is fully immobile. This is sufficient to explain that the local flux differ around the North pole between these two cases. On this example, the consequence in the global Sh is small but, at larger $Sc$ and $Re$, similar differences in the local flux of the mobile zone lead to higher discrepancies in the global $Sh$. For example, it is the case in fig. 9a for the two points of $\theta_{cap} = 0$ and $\pi/4$, at $Sc = 20$ and $Ar = 1.57 \cdot 10^3$, for which $Re$ is the same and the difference on $Sh$ is about 10%, and other examples with more significant differences can be found with the numerical results of [14]: at $Sc = 500$ and $Re = 100$, two cases at $\theta_{cap} = 0$ and 0.75 respectively give $Sh = 59.6$ and 80.4.

The global $Sh$ for contaminated bubbles can definitely not be predicted only by the knowledge of the global parameters $Re$ and $Sc$. Let us now analyze the separated contributions on the transfer flux from the immobile part (from $\theta = \theta_{cap}$ to $\pi$) and from the mobile part of the interface (integrated from $\theta = 0$ to $\theta_{cap}$), by comparing them to the integrals over the same limits for the respective cases of a solid sphere and a clean bubble used as references at same $Re$ and $Sc$.

Concerning the immobile zone of the interface, between the cases at $Ma = 1$ (partially-mobile) and $Ma = 3$ (fully-immobile) from fig. 12, at same $Sc$ and close $Re$, the mass flux integrated only from $\theta = \theta_{cap}$ to $\theta = \pi$ is smaller at $Ma = 1$ than the same integral for the solid-like case at $Ma = 3$ while the $Re$ at $Ma = 1$ is even larger by 6%. This is probably a consequence of the presence of the hydrodynamic singularity at $\theta_{cap}$ that thickens the mass boundary layer around this point, emphasized here in this case at $Ma = 1$.

Concerning the mobile zone of the interface, fig. 13 is in-

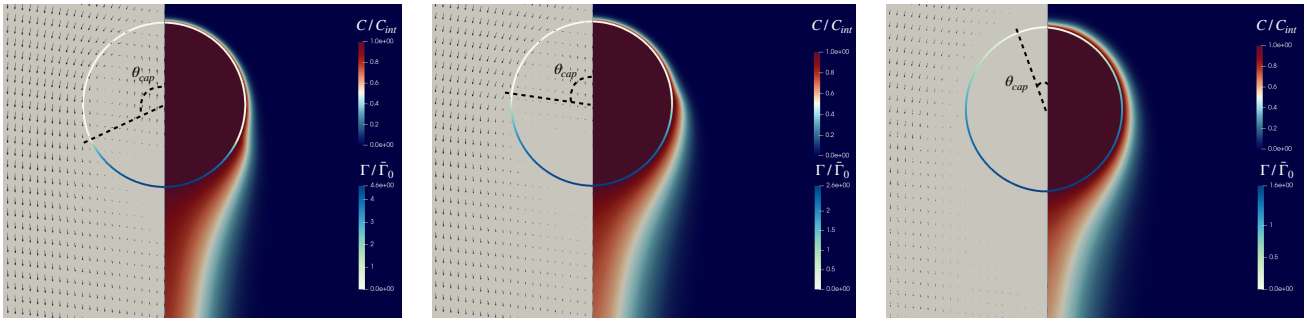


**Figure 11:** Mass transfer around a partially contaminated bubble and velocity field at $Ar = 4.28 \cdot 10^2$, $Sc = 40$ and at different Marangoni numbers : $Ma = 0.3$ on the left (leading to $Re = 15.0$), $Ma = 0.7$ ($Re = 13.0$) in the middle and $Ma = 2$ ($Re = 11.6$) on the right. Dimensionless solute concentration in the liquid and dimensionless surfactant concentration at the interface are plotted.

troduced, showing the $Sh_{loc}$ profiles of two simulations performed at same $Re$ and $Sc$ for both a clean ($Ma = 0$) and a partially contaminated bubble ($Ma = 0.7$), the global Sherwood number being different for these two cases (respectively equal to $Sh\,(Ma = 0) = 13.3$ and $Sh\,(Ma = 0.7) = 10.5$). However, even by considering only the mobile zone, for the case at $Ma = 0.7$, the mass flux integrated between $\theta = 0$ and $\theta_{cap} \approx \pi/2$ is lower than the same integral for the clean bubble, the values of $Sh_{loc}$ being smaller at each $\theta$ for the case at $Ma = 0.7$ but with a stronger decrease close to $\theta_{cap}$. Note that, for this case, the maximal velocity of the fluid at the interface is $u^*_{max} = 0.8$. For cases at larger $Ma$ which have a smaller $\theta_{cap}$ and characterized by a lower $u^*_{max}$, such a local decrease of the flux in the mobile zone more significantly impacts $Sh$ as the bubble front is the place of maximal transfer rate.

Thus, these observations prove that the global $Sh$ cannot be found by integrating the local flux of the clean bubble case from $\theta = 0$ to $\theta_{cap}$ and that of the solid sphere from $\theta = \theta_{cap}$ to $\pi$. Surprisingly, the respective contributions on the mass flux from both the surfactant-free and the covered interface zones are smaller than their respective references. This can be related to the fact that the local hydrodynamics features are impacted by the Marangoni stresses at the bubble surface: a singularity exists at the angle $\theta_{cap}$, the tangential velocity profile is modified in the remaining mobile zone, the change of its intensity being characterized by $u^*_{max}$ in particular and depending on the $\theta_{cap}$ value based on the hydrodynamic study.

### *3.2.4. Prediction of the Sherwood number*

In order to quantify the global $Sh$ for partially-contaminated bubbles, some attempts have been made in the literature, based on the knowledge of $Re$, $Sc$ and $\theta_{cap}$, but no general expression have been derived valid for all conditions.

The approach of Painmanakul et al. [41] consisted into considering that the global mass transfer rate results from a weighting system depending on the rate of surface covered by surfactants, by taking into account the global Sherwood

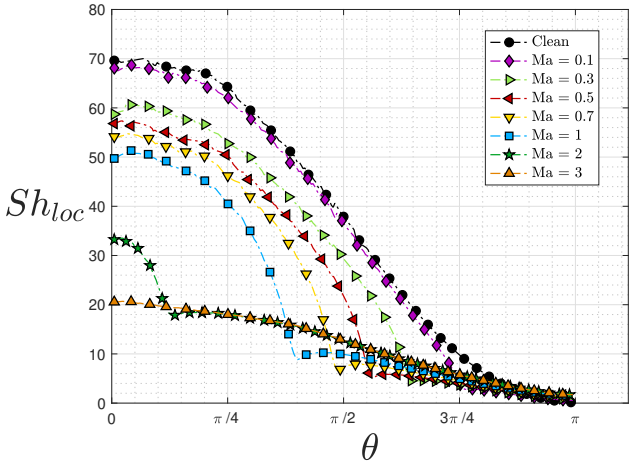


**Figure 12:** Local Sherwood number along the bubble surface at $Ar = 4.28 \cdot 10^2$, $Sc = 70$ and at different Marangoni numbers (corresponding to different Reynolds numbers). Note that, at these $Re$ values between 11 and 20, there is no recirculation vortex at the rear part of the bubble.

number of a clean bubble and a solid sphere,

$$Sh^{cont} = \alpha Sh^{solid} + (1 - \alpha) Sh^{clean} \quad , \tag{35}$$

where $\alpha$ is the rate of surface coverage. By using this approach and based on our numerical results on $Sh$, it is seen that eq. (35) always underestimates the Sherwood number values in the partially contaminated regime ($1 < \theta_{cap} < 2.5$) between 15% and 20%. Indeed, such a law provides too much weigh to the Sherwood number of a solid sphere, while the maximal intensity of transfer takes place in the front part of the partially contaminated bubble, as already highlighted from fig. 11.

Another approach was considered by Takemura and Yabe [54], who introduced the reduced Sherwood number defined in a similar way as the reduced drag coefficient,

$$Sh^* = \frac{Sh \quad - Sh^{clean}}{Sh^{solid} - Sh^{clean}} \quad . \tag{36}$$

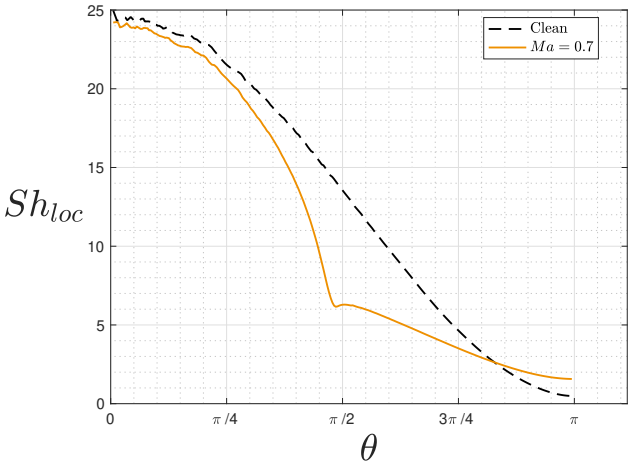


**Figure 13:** Comparison of the profile of local Sherwood between a clean bubble and a partially contaminated bubble ($\theta_{cap} = 1.49$) at same Reynolds number $Re = 13.1$ and at $Sc = 15$.

Dani et al. showed in their study [13] that, for both small

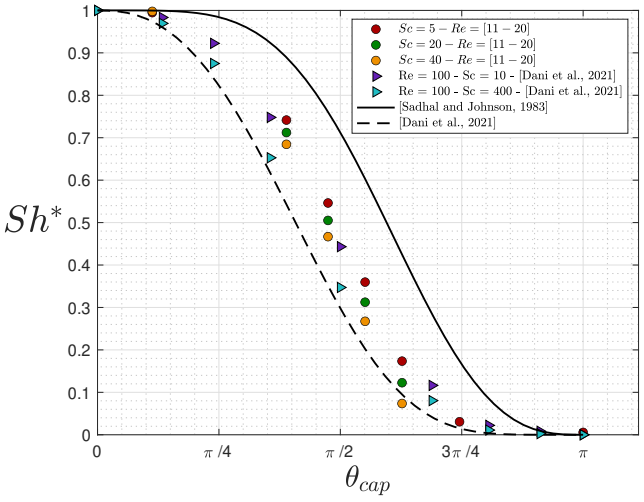


**Figure 14:** Reduced Sherwood number at $Ar = 4.28 \cdot 10^2$, comparison with the upper limit defined by equation (25) in [49] and the lower limit defined by equation (37) in [14].

Reynolds and Schmidt numbers, this reduced Sherwood number fits well with the same expression as the drag coefficient, equation (25). For higher Reynolds numbers, the authors proposed in [14] another function of $C_D^*$,

$$Sh^{*\,lower} = 1 - (1 - (C_D^*)^2)^{0.5} \quad , \tag{37}$$

to define another limit for the cases at high Schmidt numbers. The reduced Sherwood numbers of two sets of our data at two different $Ar$ values from our simulations are plotted in fig. 14. The results are in good agreement with the conclusion from Dani et al. [14] as they are well included in the two limits. This description enables a visualization of the results without the dependency on $Re$, which is involved in the two limits $Sh^{clean}$ and $Sh^{solid}$. One could consider that the contribution of the Schmidt number is also well taken into account in these limiting values, as the scaling laws of the mass boundary layers in the case of a clean bubble and a solid sphere are included in the corresponding correlations. However, fig. 14 and results from [14] prove that an impact of this parameter is remaining as the points are dispersed in between the two limits depending on the $Sc$ value, and this spreading is larger for intermediate values of $\theta_{cap}$ than for low or high $\theta_{cap}$ angles. Consequently, considering a reduced Sherwood number $Sh^*$ may not be the easier and most appropriate parameter to establish a general correlation.

An alternative for the prediction of the global $Sh$ is now proposed, by combining global and local parameters. For both a clean bubble and a solid particle, the scaling of the mass boundary layer thickness in eq. (29) and (32) reveals that the Reynolds number is always involved with a power of $1/2$. However, the contribution of the Schmidt number varies between $Sc^{1/2}$ and $Sc^{1/3}$ for these two extreme cases and, in between, it has been shown in the previous section that the contribution of the Schmidt number (at same $Re$) can be quantified as a function of the contamination angle $Sc^{f(\theta_{cap})}$, with $f(\theta_{cap})$ an increasing function from $1/3$ to $1/2$. In addition, to predict $Sh$ for partially contaminated bubbles, it is also necessary to take into account the change in the local hydrodynamics which depends on the contamination angle and that can significantly impact the local transfer rate in both the mobile and the immobile part of the interface, as emphasized from the analysis of the local fluxes around the interface. In this work, it is proposed to quantify the impact of surfactants on the hydrodynamics through the ratio $u^*_{max}$ of the maximal fluid velocity at the interface over its value for a clean bubble, this dimensionless ratio being a function of $\theta_{cap}$ and varying between 0 and 1.

In this way, by gathering all the effects analyzed previously, the following expression is proposed to predict the dimensionless global mass flux around a contaminated bubble

$$Sh^{cont} = 2 + Re^{1/2}\, Sc^{f(\theta_{cap})} \left[ {u^*_{max}}^{1.5} \frac{2}{\sqrt{\pi}}\, g^{clean} + \left(1 - u^*_{max}\right)^{1.2} g^{solid} \right] \left(1 - u^*_{max}\right)^{1.2} \quad , \tag{38}$$

with

$$g^{clean} = \left(1 - \frac{2}{3}\frac{1}{(1+0.09Re^{2/3})^{1.1}}\right)^{0.45}, \quad (39)$$

$$g^{solid} = Re^{-0.09}\left(1 + \frac{1}{Re\,Sc}\right)^{1/3}, \quad (40)$$

$$f(\theta_{cap}) = \frac{1}{3} - 0.014\,\theta_{cap}^2 + \frac{1}{\pi}\left(\frac{1}{6} + 0.014\pi^2\right)\theta_{cap}\ . \quad (41)$$

The function $f$, used as exponent of $Sc$, in eq. (41), ensures a continuous transition of the thickness of the mass boundary layer from that around a clean interface to an immobile surface. Note that $f(\theta_{cap})$ is found to be more relevant than a function of $u^*_{max}$ to reproduce the variations of $Sh$ as a function of $Sc$, when including all the simulation points.

The expression given by eq. (38) ensures that the Sherwood number tends towards the limit of the $Sh$ for a solid sphere by means of $g^{solid}$ when $\theta_{cap} \to 0$ for which $u^*_{max} = 0$, and towards the limit of the clean bubble thanks to $g^{clean}$ when $\theta_{cap} \to \pi$ for which $u^*_{max} = 1$. On the one hand, the function $g^{solid}$ comes from the prediction of eq.(33) from Clift et al. [9], and brings a small correction in $Re$ and $Pe$ to the main evolution of $Sh^{solid}$ as $Re^{1/2}Sc^{1/3}$. On the other hand, $g^{clean}$ is another function based on eq.(30) from Takemura and Yabe [53]. Such a writing permits that $Sh$ tends towards the prediction from the potential theory of Boussinesq [7] for a clean bubble when $Re$ and $Pe$ tends towards infinite, and $g^{clean}$ is used to correct the main evolution of $Sh^{clean}$ as $Pe^{1/2}$ at moderate $Re$. However, note that $g^{clean}$ corresponds here to a slightly modified expression as compared to the original correction term proposed in [53] for clean bubbles: it ensures that the prediction of $Sh^{clean}$ when $u^*_{max} = 1$ in eq. (38) is closer to the correlation proposed by Colombet et al. [10] at large $Re$ and $Sc$ in the fully mobile case (the discrepancy between all these expressions being only of a few percents), and it allows to obtain a better fit of all the simulation points.

Between the two limits $g^{clean}$ and $g^{solid}$, the parameter $u^*_{max}$ acts as a weigh and ensures the transition between the clean bubble and the solid sphere pre-factors for intermediate contamination angles.

All numerical data from this study (contaminated bubbles by including the extreme cases of clean bubble and the fully-contaminated one), those of [54] at $Sc = 500$ and $10 \leq Re \leq 100$ for partially-contaminated bubbles and those of [14] at $1 \leq Sc \leq 500$ and $1 \leq Re \leq 100$ are plotted in fig. 15. A very good agreement is obtained with eq.(38), which permits to gather all the results under a single formulation in a very large range of physical parameters (more than 4 orders of magnitude of variation of Pe, and whatever the angle of contamination), with a maximal discrepancy of 10 % and a coefficient correlation of 0.99. In particular, this correlation is relevant to deal with experimental cases of gas-liquid mass transfer at very high Schmidt numbers.

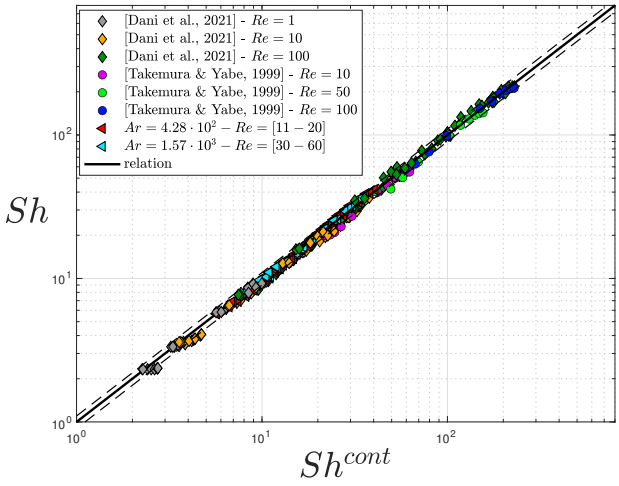


**Figure 15:** Proposed correlation for the Sherwood number around contaminated bubbles, eq. 38 (combined with eq. (27) for $u^*_{max}$), compared to simulations from this study and data from numerical works [54] and [14]. Lines −− corresponds to limits 10% above and below the proposed correlation. The correlation is validated for $1 \leq Re \leq 100$, $1 \leq Sc \leq 500$ and all $\theta_{cap}$ values from 0 to $\pi$.

As it was mentioned by Colombet et al. [10] in the case of a clean bubble, the maximum fluid velocity at the interface is appropriate to describe the mass transfer, and it is shown in this paper that it is also relevant in the case of a contaminated bubble in the stagnant-cap regime. This study therefore brings a new highlight in the role of $u_{max}$ : this maximal tangential velocity can be used to quantify the regulation of the mass transfer intensity for partially contaminated bubbles between the rate of a clean bubble and a solid particle, by valuing the contribution from the front part free of surfactants where the main transfer rate takes place.

Note that the proposed correlation is valid without distinguishing the cases where a vortex is present at the bubble rear or not, similarly to the transfer rate correlations around solid particles. Indeed, as mentioned by [14] for bubbles with partially mobile interface, flow separation occurs at an angle which depends on $\theta_{cap}$ for $Re \geq 20$. However, eq. (38) shows that such detail on the hydrodynamics is not required for the prediction of the global mass transfer rate around partially contaminated bubbles.

## 4. Conclusion and perspectives

In this paper, Direct Numerical Simulations have been performed to study the influence of surfactants on mass transfer around bubbles in the stagnant-cap regime. The cou-

pling between the hydrodynamics and the Marangoni effect is solved so that the numerical configuration corresponds to the experimental conditions of rising bubbles with different concentrations of adsorbed surfactants, where $Re$ and $\theta_{cap}$ are not imposed but obtained as results. Computation of the hydrodynamics have first been validated through comparisons on the drag coefficient with previous studies. Then, a local analysis has enabled to predict the decrease of the maximum velocity for the fluid at the interface, that is found to depend only on the angle of contamination in the investigated range of Reynolds numbers $O(10-100)$, and which is shown to be one relevant parameter to quantify the mass transfer rate around these contaminated bubbles. A general correlation, eq. 38, has finally been proposed to quantify the Sherwood number between the two limits of the clean and solid-like bubbles in a very large range of $Re$ and $Sc$. It permits to gather all the cases at any coverage rate of the interface, and $Sh$ depends on both global and local parameters: the Reynolds number $Re$, the Schmidt number $Sc$, the angle of contamination $\theta_{cap}$, and the normalized maximum surface velocity $u^*_{max}$. For practical purpose, based on results of the present investigation, $u^*_{max}$ can be predicted by using the correlation eq.(27), which requires only $\theta_{cap}$ as input, the latter being a crucial parameter to characterize the hydrodynamics in the stagnant-cap regime. $\theta_{cap}$ can be estimated from fig. 3 or fig. 6, by knowing either the rise velocity of the contaminated bubble (then computing the drag coefficient) or the amount of adsorbed surfactants at the interface (the latter can be evaluated by measuring the time scales of the bubble shape oscillation for example, as proposed in [28]).

The parametric study reveals the strong transfer rate drop when a bubble is partially contaminated, as compared to the case of a clean bubble at same $Ar$ and $Sc$. This decrease can finally be explained by the coupling between (i) the bubble velocity decrease induced by the Marangoni effect ($Re$ is reduced), and (ii), even at same $Re$, local phenomena which depend on the angle of contamination $\theta_{cap}$: when a part of the interface is immobilized, first, the mass boundary layer is thicker in this zone, globally resulting in a lower contribution of the Schmidt number which makes $Sh$ to decrease, secondly the local hydrodynamics in the mobile zone is also affected and contributes again to a decrease of $Sh$, such impact being characterized by a reduction of the tangential velocity $u^*_{max}$. Note that $Sh$ is mainly sensitive to the hydrodynamic condition in the front part of the interface since it is the region of maximal contribution in the total transfer rate.

In this investigation, no bubble volume decrease due to mass transfer has been considered. The prediction of the mass transfer coefficient in steady conditions, around a bubble of given size, is however relevant to model the slow dissolution of gas bubbles, as a quasi-steady process [56, 38]. Regarding the impact of surfactants, the present study can be considered as a first stage in the understanding of the transfer decrease in the presence of soluble surfactants leading to the stagnant-cap regime, reached here under the insoluble limit (no adsorption/desorption fluxes). A description of the transient adsorption and desorption processes of soluble surfactants, allowing for a complete comparison between experimental and numerical results, would be complementary to this work.

## Acknowledgements

This work was granted access to the HPC resources of CALMIP supercomputing center under the allocation 2020-[P19066] and 2021-[P19066].

The authors would like to acknowledge the financial support provided by Région Occitanie. This research was carried out in collaboration with the FERMaT federation.

The authors acknowledge Pr. Anne-Marie Billet and Pr. Pascal Guiraud for fruitful discussions on the results.

## CRediT authorship contribution statement

**Kalyani Kentheswaran:** Conceptualization, Methodology, Software, Validation, Investigation, Data curation, Writing - original draft, Writing - review & editing, Visualization. **Nicolas Dietrich:** Conceptualization, Validation, Writing - review & editing, Funding acquisition, Supervision, Project administration. **Sébastien Tanguy:** Software, Validation, Writing - review & editing. **Benjamin Lalanne:** Conceptualization, Methodology, Software, Validation, Investigation, Writing - review & editing, Funding acquisition, Supervision, Project administration.

## References

[1] Abadie, T., al Ma Awali, S.M., Brennan, B., Briciu-Burghina, C., Tajparast, M., Passos, T.M., Durkan, J., Holland, L., Lawler, J., Nolan, K., Quilty, B., Fitzsimons, L., Regan, F., Delauré, Y., 2022. Oxygen transfer of microbubble clouds in aqueous solutions – application to wastewater. Chemical Engineering Science 257, 117693. URL: https://www.sciencedirect.com/science/article/pii/S0009250922002779, doi:https://doi.org/10.1016/j.ces.2022.117693.

[2] Aslam, T., 2003. A partial differential equation approach to multidimensional extrapolation. Journal of Computational Physics 193, 349–355.

[3] Bel Fdhila, R., Duineveld, P., 1996. The effect of surfactant on the rise of a spherical bubble at high reynolds and peclet numbers. Physics of Fluids 8, 310–321.

[4] Borges, R., Carmona, M., Costa, N., Don, W.S., 2008. An improved weighted essentially non-oscillatory scheme for hyperbolic conservation laws. Journal of Computational Physics 227, 3191–3211.

[5] Bothe, D., 2022. Sharp-interface continuum thermodynamics of multicomponent fluid systems with interfacial mass. International Journal of Engineering Science 179, 103731. URL: https://www.sciencedirect.com/science/article/pii/S0020722522001008, doi:https://doi.org/10.1016/j.ijengsci.2022.103731.

[6] Bothe, D., Fleckenstein, S., 2013. A volume-of-fluid-based method for mass transfer processes at fluid particles. Chemical Engineering Science 101, 283–302.

[7] Boussinesq, J., 1905. Calcul du pouvoir refroidissant des courants fluides. Journal de Mathématiques Pures et Appliquées 6.

[8] Butler, C., Cid, E., Billet, A.M., Lalanne, B., 2021. Numerical simulation of mass transfer dynamics in taylor flows. International Journal of Heat and Mass Transfer 179.

[9] Clift, R., Grace, J., Weber, M., 1978. Bubbles, Drops and Particles. Academic Press, New York.

[10] Colombet, D., Legendre, D., Cockx, A., Guiraud, P., 2013. Mass or heat transfer inside a spherical gas bubble at low to moderate reynolds number. International Journal of Heat and Mass Transfer 67.

[11] Cuenot, B., Magnaudet, J., Spennato, B., 1997. The effects of slightly soluble surfactants on the flow around a spherical bubble. Journal of Fluids Mechanics 339.

[12] Dalmon, A., Kentheswaran, K., Mialhe, G., Lalanne, B., Tanguy, S., 2020. Fluids-membrane interaction with a full eulerian approach based on the level set method. Journal of Computational Physics 406.

[13] Dani, A., Cockx, A., Guiraud, P., 2006. Direct numerical simulation of mass transfer from spherical bubbles : the effect of interface contamination at low reynolds number. Journal of Chemical Reactor Engineering 4.

[14] Dani, A., Cockx, A., Legendre, D., Guiraud, P., 2021. Effect of spheroid bubble interface contamination on gas-liquid mass transfer at intermediate reynolds numbers: from dns to sherwood numbers. Chemical Engineering Science In press.

[15] Dendy, J., 1982. Black box multigrid. Journal of Computational Physics 48.

[16] Fedkiw, R., Aslam, T., Merriman, B., Osher, S., 1999. A Non-oscillatory Eulerian Approach to Interfaces in Multimaterial Flows (the Ghost Fluid Method). Journal of Computational Physics 152.

[17] Figueroa-Espinoza, B., Legendre, D., 2010. Mass or heat transfer from spheroidal gas bubbles rising through a stationary liquid. Chemical Engineering Science 65, 6296–6309.

[18] Fleckenstein, S., Bothe, D., 2013. Simplified modeling of the influence of surfactants on the rise of bubbles in vof-simulations. Chemical engineering science 102, 514–523.

[19] Frumkin, A., Levich, V., 1947. On surfactants and interfacial motion. Zhur. Fiz. Khim. 21, 1183.

[20] Gibou, F., Fedkiw, R.P., Cheng, L., Kang, M., 2002. A second-order-accurate symmetric discretization of the poisson equation on irregular domains. Journal of Computational Physics 176, 205–227.

[21] Higbie, R., 1935. The rate of absorption of a pure gas into a still liquid during short periods of exposure. Trans. AIChE 31.

[22] Horton, T.J., Fritsch, T.R., Kintner, R.C., 1965. Experimental determination of circulation velocities inside drops. The Canadian Journal of Chemical Engineering 43, 143–146.

[23] Jia, H., Zhang, P., 2017. Mass transfer of a rising spherical bubble in the contaminated solution with chemical reaction and volume change. International Journal of Heat and Mass Transfer 110.

[24] Jimenez, M., Dietrich, N., Grace, J., Hebrard, G., 2014. Oxygen mass transfer and hydrodynamic behaviour in wastewater: Determination of local impact of surfactants by visualization techniques. Water Research 58.

[25] Kang, M., Fedkiw, R., Liu, X.D., 2000. A boundary condition capturing method for multiphase incompressible flow. Journal of Scientific Computing 15, 323–360.

[26] Lalanne, B., Abi Chebel, N., Vejražka, J., Tanguy, S., Masbernat, O., Risso, F., 2015a. Non-linear shape oscillations of rising drops and bubbles: Experiments and simulations. Physics of Fluids 27.

[27] Lalanne, B., Masbernat, O., Risso, F., 2020a. Determination of interfacial concentration of a contaminated droplet from shape oscillation damping. Physical Review Letters 124.

[28] Lalanne, B., Masbernat, O., Risso, F., 2020b. Determination of interfacial concentration of a contaminated droplet from shape oscillation damping. Physical Review Letters 124, 194501.

[29] Lalanne, B., Rueda Villegas, L., Tanguy, S., Risso, F., 2015b. On the computation of viscous terms for incompressible two-phase flows with Level Set/Ghost Fluid Method. Journal of Computational Physics 301.

[30] Lebrun, G., Xu, F., Le Men, C., Hébrard, G., Dietrich, N., 2021. Gas–liquid mass transfer around a rising bubble : combined effect of rheology and surfactant. Fluids 84.

[31] Legendre, D., 2007. On the relation between the drag and the vorticity produced on a clean bubble. Physics of Fluids 19.

[32] Lepilliez, M., Popescu, E.R., Gibou, F., Tanguy, S., 2016. On two-phase flow solvers in irregular domains with contact line. Journal of Computational Physics 321.

[33] Levich, V.G., 1962. Physicochemical Hydrodynamics. Prentice-Hall, New York.

[34] Lochiel, A.C., Calderbank, P.H., 1964. Mass transfer in the continuous phase around axisymmetric bodies of revolution. Chemical Engineering Science 19, 4.

[35] Madhavi, T., Golder, A., Samanta, A., Ray, S., 2007. Studies on bubble dynamics with mass transfer. Chemical Engineering Journal 128.

[36] Mei, R., Klausner, J.F., Lawrence, C.J., 1994. A note on the history force on a spherical bubble at finite reynolds number. Physics of Fluids 418.

[37] Mougin, G., Magnaudet, J., 2002. The generalized kirchoff equations and their application to the interaction between a rigid body and an arbitrary time-dependent viscous flow. International Journal of Multiphase Flow 28.

[38] Olsen, J.E., Dunnebier, D., Davies, E., Skjetne, P., Morud, J., 2017. Mass transfer between bubbles and seawater. Chemical Engineering Science 161, 308–315.

[39] Orazzo, A., Tanguy, S., 2019. Direct numerical simulations of droplet condensation. International Journal of Heat and Mass Transfer 129.

[40] Osher, S., Sethian, J., 1988. Fronts propagating with curvature-dependent speed: Algorithms based on hamilton-jacobi formulations. Journal of Computational Physics 79, 12–49.

[41] Painmanakul, P., Loubière, K., Hébrard, G., Mietton-Peuchot, M., Roustan, M., 2005. Effect of surfactants on liquid-side mass transfer coefficients. Chemical Engineering Science 60.

[42] Palaparthi, R., Demetrios, T.P., Maldarelli, C., 2006. Theory and experiments on the stagnant cap regime in the motion of spherical surfactant-laden bubbles. Journal of Fluids Mechanics 559.

[43] Pereira, A., Kalliadasis, S., 2008. On the transport equation for an interfacial quantity. The European Physical Journal Applied Physics 44, 211–214.

[44] Pesci, C., Weiner, A., Marschall, H., Bothe, D., 2018. Computational analysis of single rising bubbles influenced by soluble surfactant. Journal of Fluid Mechanics 856.

[45] Piedfert, A., Lalanne, B., Masbernat, O., Risso, F., 2018. Numerical simulations of a rising drop with shape oscillations in the presence of surfactants. Physical Review Fluids 3.

[46] Rueda Villegas, L., Alis, R., Lepilliez, M., Tanguy, S., 2016. A ghost fluid/level set method for boiling flows and liquid evaporation: application to the leidenfrost effect. Journal of Computational Physics 316.

[47] Rueda Villegas, L., Tanguy, S., Castanet, G., Caballina, O., Lemoine, F., 2017. Direct numerical simulation of the impact of a droplet onto a hot surface above the leidenfrost temperature. International Journal of Heat and Mass Transfer 104, 1090–1109.

[48] Saboni, A., Alexandrova, S., Spasic, A., Gourdon, C., 2007. Effect of the viscosity ratio on mass transfer from a fluid sphere at low to veryhigh peclet numbers. Chemical Engineering Science 62, 4742–4750.

[49] Sadhal, S., Johnson, S., 1983. Stokes flow past bubbles and drops partially coated with thin films. part 1 : Stagnant cap of surfactant filmexact solution. Journal of Fluids Mechanics 126.

[50] Stone, H.A., 1990. A simple derivation of the time-dependent convective-diffusion equation for surfactant transport along a deforming interface. Physics of Fluids 111.

[51] Sussman, M., Smereka, P., Osher, S., 1994. A level set approach for computing solutions to incompressible two-phase flow. Journal of Computational Physics 114, 146–159.

[52] Takagi, S., Matsumoto, Y., 2011. Surfactant effects on bubble motion and bubbly flows. Annual Review of Fluid Mechanics 43, 615–636.

[53] Takemura, F., Yabe, A., 1998. Gas dissolution process of spherical rising bubbles. Chemical Engineering Science 53, 2691–2699.

[54] Takemura, F., Yabe, A., 1999. Rising speed and dissolution rate of a carbon dioxide bubble in slightly contaminated water. Journal of Fluids Mechanics 334.

[55] Takemura, F., Yabe, A., 2005. Adsorption of surfactants onto the surface of a spherical rising bubble and its effect on the terminal velocity

of the bubble. Physics of Fluids 17.

[56] Tanaka, S., Kastens, S., Fujioka, S., Schlüter, M., Terasaka, K., 2020. Mass transfer from freely rising microbubbles in aqueous solutions of surfactant or salt. Chemical Engineering Journal 387, 121246.

[57] Tanguy, S., Menard, T., Berlemont, A., 2007. A level set method for vaporizing two-phase flows. Journal of Computational Physics 221.

[58] Tanguy, S., Sagan, M., Lalanne, B., Couderc, F., Colin, C., 2014. Benchmarks and numerical methods for the simulation of boiling flows. Journal of Computational Physics 264, 1–22.

[59] Urbano, A., Tanguy, S., Colin, C., 2019. Direct numerical simulation of nucleate boiling in zero gravity conditions. International Journal of Heat and Mass Transfer 143.

[60] Valkovska, D.S., Danov, K.D., 2000. Determination of bulk and surface diffusion coefficients from experimental data for thin liquid film drainage. Journal of colloid and interface science 223, 314–316.

[61] Vasconcelos, J.M.T., Orvalho, S.P., Alves, S.S., 2002. Gas-liquid mass transfer to single bubbles : effect of surface contamination. AIChE Journal 48.

[62] Weiner, A., Bothe, D., 2017. Advanced subgrid-scale modeling for convection-dominated species transport at fluid interfaces with application to mass transfer from rising bubbles. Journal of Computational Physics 347, 261–289.

[63] Xu, F., Hébrard, G., Dietrich, N., 2020. Comparison of three different techniques for gas-liquid mass transfer visualization. International Journal of Heat and Mass Transfer 150.

[64] Xu, J.J., Zhao, H.K., 2003. An eulerian formulation for solving partial differential equations along a moving interface. Journal of Scientific Computing 19, 573–594.